

FUMO: Prior-Modulated Diffusion for Single Image Reflection Removal

Telang Xu^{1,*}, Chaoyang Zhang^{2,3,*}, Guangtao Zhai¹, and Xiaohong Liu^{1,2,†}

¹ Shanghai Jiao Tong University

² Shanghai Innovation Institute

³ Xi'an Jiaotong University

{luciousdesmon, xiaohongliu, zhaiguangtao}@sjtu.edu.cn

{zcyxjtu65}@gmail.com

*Equal Contribution †Corresponding author

Abstract. Single image reflection removal (SIRR) is challenging in real scenes, where reflection strength varies spatially and reflection patterns are tightly entangled with transmission structures. This paper presents a diffusion model with prior modulation framework (FUMO) that introduces explicit guidance signals to improve spatial controllability and structural faithfulness. Two priors are extracted directly from the mixed image, an intensity prior that estimates spatial reflection severity and a high-frequency prior that captures detail-sensitive responses via multi-scale residual aggregation. We propose a coarse-to-fine training paradigm. In the first stage, these cues are combined to gate the conditional residual injections, focusing the conditioning on regions that are both reflection-dominant and structure-sensitive. In the second stage, a fine-grained refinement network corrects local misalignment and sharpens fine details in the image space. Experiments conducted on both standard benchmarks and challenging images in the wild demonstrate competitive quantitative results and consistently improved perceptual quality. The code is released at <https://github.com/Lucious-Desmon/FUMO>.

Keywords: Reflection removal · Conditional generation · Diffusion model

1 Introduction

Images captured through glass or other transparent media often contain unwanted reflections that obscure the underlying scene [37, 51]. Such artifacts degrade visual quality and hinder downstream vision applications [28, 38]. Reflection removal aims to suppress reflections and recover a clear transmission image from a mixture input. The task in real-world settings remains challenging due to severe layer entanglement and large spatial variations in reflection appearance [7, 14, 62].

Methods [1, 8, 20, 35, 36, 50, 52] leveraging multiple images depend on specialized acquisition and are less applicable to casual photography or internet images.

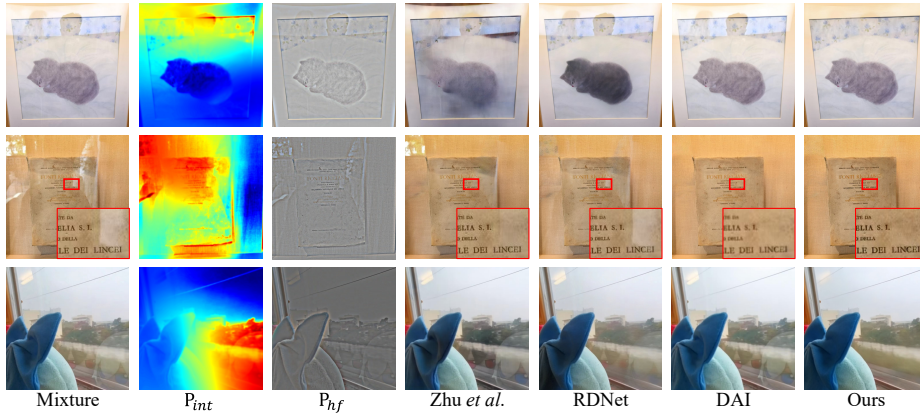


Fig. 1: Failure-mode visualization on in-the-wild reflection mixtures. Three representative real-world mixed images are shown together with two priors. Qualitative comparisons with representative SOTA methods illustrate common challenges in the wild, including incomplete reflection suppression, color inconsistency, and loss of fine details. Red rectangles highlight regions for closer inspection.

In the single-image task, traditional optimization methods [2, 19, 21, 34, 49, 59, 60] impose hand-crafted priors to decompose layers, yet they are often brittle when assumptions are violated and computationally expensive. Learning-based approaches [7, 11, 13, 14, 22, 23, 45, 58, 60, 62] improve performance by learning deep priors from data, but robust reflection removal in the wild remains challenging. More recently, diffusion models [11, 12, 26, 41, 47, 61] have shown strong potential for image restoration, which calls for appropriate guidance conditions to avoid undesired content drift and structural distortions. Overall, reflection removal faces an intrinsic trade-off, the tension between aggressive reflection suppression and faithful preservation of scene structure under large reflection variability. In practice, this trade-off manifests as three common issues on real mixtures, including incomplete reflection suppression, color inconsistency, and loss of fine details, as illustrated in Fig. 1.

To address this, we introduce an explicit and controllable mechanism that suppresses reflection strength spatially and preserves scene structure. We derive two complementary priors to enable spatially grounded guidance, a vision-language model (VLM) [3, 24, 42, 44] based reflection intensity prior and a high-frequency prior by multi-scale residual decomposition. Examples of the priors P_{int} and P_{hf} are shown in Fig. 1. The intensity prior captures both region-level reflection analysis and global localization of reflection phenomena, thereby indicating where reflection removal should be stronger and to what extent. The high-frequency prior, in turn, provides a detailed sensitive signal that helps the model remain attentive to local structures during restoration. We integrate these priors into a spatial gate, which provides a coherent guidance map and enables spatially selective modulation of the conditioning strength.

Building on these guided priors, we propose **FUMO**, a dif**F**usion model with prior **MO**dulation framework for SIRR, which adopts a coarse-to-fine design. In the first stage, a conditional diffusion model [33, 55] is guided by the proposed gate to aggressively remove reflections, driving the low frequency appearance toward the underlying transmission content. This stage delivers effective reflection removal, but strong suppression can still introduce geometric deviations or local inconsistencies. We therefore follow with a fine-grained refinement module, combined with the two priors, to correct distortions and restore coherent structures and details. Experiments demonstrate that our approach achieves strong performance under diverse scenes.

The main contributions are summarized as follows:

- We introduce a practical pipeline to obtain two priors that provide spatial guidance for reflection removal, supporting both reflection strength estimation and detail aware guidance.
- We propose a coarse-to-fine framework that jointly enhances reflection attenuation and reconstruction fidelity, producing outputs that are cleaner and more geometrically consistent.
- Extensive experiments on standard benchmarks and challenging in-the-wild images demonstrate that the proposed approach achieves strong results and compares favorably with state of the art methods.

2 Related Work

2.1 Image Reflection Removal

Due to the complex superposition of the transmission and reflection layers, recovering the transmission from a single blended image is a mathematically ill-posed problem. An intuitive solution is Multi-Image Reflection Removal (MIRR) [1, 8, 20, 35, 36, 50, 52], which utilizes auxiliary information from multiple images, such as dynamic scenes [35], focused/defocused images [36], or polarization imaging [20, 52]. These methods mitigate reflection interference through comparative analysis and can effectively alleviate the ill-posed nature of the problem. However, their reliance on specific equipment or capture conditions limits their practical applicability, especially when processing existing images on the Internet or for mobile devices [11].

In contrast, Single-Image Reflection Removal (SIRR) [51] aims to tackle this problem by exploring intrinsic priors from a single input. Some works relied on hand-crafted priors [2, 19, 21, 34, 49, 59, 60], such as edge annotations [21], ghosting cues [34], and sparsity assumptions [2]. With the development of deep learning, neural network-based methods [7, 11, 13, 14, 22, 23, 45, 58, 60, 62] have demonstrated superior performance and lower costs by autonomously learning implicit priors from the blended image. Dong *et al.* [7] design a reflection detection module to regress a probabilistic reflection confidence map. YTMT [13] enforces the predictions to communicate with each other. DSRNet [14] proposes DSFFNet to initially extract transmission and reflection features. Zhu *et al.* [62] introduces

MaxRF to explicitly indicate virtual objects. RDNet [58] employs a reversible encoder to secure valuable information. SIRR methods increasingly incorporate reflection localization and structure preserving designs to improve robustness in real scenes. Following this direction, we leverage explicit reflection strength priors together with detail oriented guidance to improve controllability and fidelity in reflection removal.

2.2 Diffusion Models

In recent years, diffusion models have achieved significant progress. DDPM [10] establishes a powerful new paradigm and has sparked extensive follow up research. DDIM [29] further improves sampling efficiency by enabling a more flexible generation procedure. Latent diffusion models (LDMs) [32, 33] conduct the diffusion process in a compact latent space and facilitate the integration of additional conditioning signals, which significantly broadens their applicability. In addition to U-Net denoisers, studies also explore diffusion transformer denoisers [31], further enriching architectural choices. These developments collectively strengthen the generative prior of diffusion models and provide flexible design choices for downstream tasks.

Building on their success in generation, diffusion models have been adapted for image enhancement and restoration, demonstrating powerful capabilities in tasks such as low-light enhancement [61], dehazing [41], and super-resolution [26, 47]. In reflection removal, L-Differ [11] first introduces diffusion models to this task, where previous predictions are used as conditions to steer an iterative denoising process. DAI [12] strengthens conditional injection with a ControlNet and further improves reconstruction with a refined decoder. PolarFree [52] leverages diffusion based modeling to produce reflection free imaging priors, which support subsequent reflection suppression. These advances suggest that diffusion models are promising for dereflection, and effective results often rely on appropriate conditioning and guidance to preserve faithful transmission content. Motivated by this insight, our framework adopts a diffusion backbone and combines explicit guidance with a dedicated structural refinement module.

3 Methods

The core of this work is to leverage a pretrained VLM to extract guidance priors that provide spatial cues for single image reflection removal, improving detail preservation and color consistency in the recovered transmission. The overall framework is illustrated in Fig. 3.

In this section, we begin by extracting two complementary priors, an intensity prior and a high-frequency prior, which are introduced in Sec. 3.1. These priors are then converted into a spatial gate and injected into the diffusion denoising U-Net to perform coarse restoration, while a lightweight refinement module further improves geometric consistency and detail coherence. The full architecture is described in Sec. 3.2. Finally, the training losses are provided in Sec. 3.3.

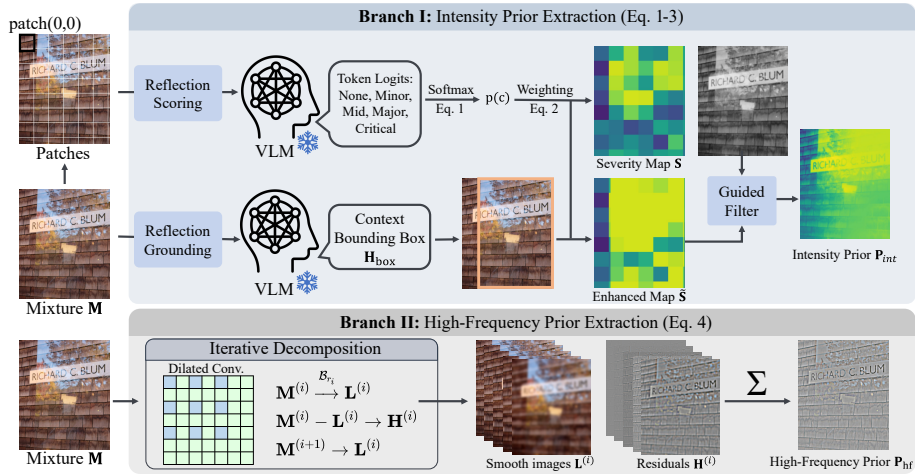


Fig. 2: The pipeline of dual prior extraction. In branch I, the mixed image \mathbf{M} is divided into patches, and the intensity prior \mathbf{P}_{int} is finally obtained through scoring and localization. In branch II, the mixed image \mathbf{M} is iteratively decomposed and aggregated to yield the high-frequency prior \mathbf{P}_{hf} .

3.1 Dual Prior Extraction

The mixed image alone usually lacks sufficient cues to robustly separate reflections from transmission structures. To alleviate this limitation, we extract two complementary priors, an intensity prior and a high-frequency prior from the mixed image. The overall prior extraction pipeline is shown in Fig. 2.

Reflection Intensity Prior. The rapid development of Vision Language Models (VLMs) [3, 24, 42, 44] provides a practical way to extract richer and more generalizable priors from a mixed image. Studies such as [5, 27, 46, 61] suggest that VLM derived signals, including intermediate reasoning outputs, can benefit image analysis and processing. Building on this capability, we use a VLM to produce a reflection intensity prior that indicates where reflection interference is stronger and to what extent. Given a mixed image \mathbf{M} , the reflection intensity prior $\mathbf{P}_{\text{int}} \in [0, 1]^{H \times W}$ is a pixel-level map to provide spatially grounded guidance for subsequent conditioning.

We start from patch-level severity scoring to capture local reflection evidence at a manageable granularity. Inspired by Q-ALIGN [46], we partition \mathbf{M} into non-overlapping patches (with patch size a chosen adaptively according to image resolution), and query a VLM to assess reflection severity using a fixed ordinal set $\mathcal{C} = \{\text{None}, \text{Minor}, \text{Mid}, \text{Major}, \text{Critical}\}$. Instead of relying on free-form text outputs, we exploit the model’s next-token logits and restrict the probability mass to \mathcal{C} , yielding a more stable confidence distribution over the predefined

levels:

$$p(c) = \frac{\exp(\ell(c)/\tau)}{\sum_{c' \in \mathcal{C}} \exp(\ell(c')/\tau)}, \quad c \in \mathcal{C}, \quad (1)$$

where $\ell(c)$ denotes the logit of the token corresponding to category c and τ is a temperature. Then a continuous severity score is obtained through an ordinal expectation with weights $w(c) \in \{1, 2, 3, 4, 5\}$:

$$s = \sum_{c \in \mathcal{C}} w(c) p(c). \quad (2)$$

We bring the patch scores back to the image plane to form a pixel-wise field \mathbf{S} by assigning the same score to all pixels within each patch.

Patch-level scoring provides robust local estimates, but may overlook reflection regions that are visually prominent on the global scale. We further perform image level analysis on the mixed image \mathbf{M} . Similarly to region localization in object detection, we prompt the VLM to identify areas dominated by reflections and return their bounding boxes. Then the corresponding regions in \mathbf{S} is boosted with a multiplicative factor to obtain an enhanced map $\tilde{\mathbf{S}}$ (capped by a maximum value), which better captures large, coherent reflection patterns without altering the underlying patch scoring mechanism.

Subsequently, we densify $\tilde{\mathbf{S}}$ into a spatially coherent guidance map via an edge-aware guided filter [9]:

$$\mathbf{P}'_{\text{int}} = \text{GF}(\tilde{\mathbf{S}}; \mathbf{G}, r, \epsilon), \quad (3)$$

where the guide image \mathbf{G} is obtained from \mathbf{M} by converting to grayscale and applying a mild Gaussian pre-blur. This step removes block artifacts while encouraging intensity transitions to align with major image structures. Ultimately, we clamp the filtered response to a fixed range and linearly rescale it to $[0, 1]$ to obtain the final intensity prior \mathbf{P}_{int} , aligned with the input resolution.

High-Frequency Prior. The intensity prior provides spatial awareness of reflection strength. To complement it with a detail sensitive signal, we further extract a high-frequency prior from the same mixture input. The prior serves as a direct cue that encourages the model to remain attentive to local details during restoration. Since it is extracted from the mixture \mathbf{M} , the prior contains high-frequency components from both layers and is therefore used only for guidance.

Given the mixed image \mathbf{M} , we construct a multi-scale residual decomposition inspired by wavelet color correction [40] to compute the high-frequency prior \mathbf{P}_{hf} . Let $\mathcal{B}_r(\cdot)$ denote a channel-wise smoothing operator at scale r , implemented with dilated convolution [54]. Starting from $\mathbf{M}^{(0)} = \mathbf{M}$, we iteratively compute a smoothed image and its residual at increasing scales: $\mathbf{L}^{(i)} = \mathcal{B}_{r_i}(\mathbf{M}^{(i)})$, $\mathbf{H}^{(i)} = \mathbf{M}^{(i)} - \mathbf{L}^{(i)}$, and update $\mathbf{M}^{(i+1)} = \mathbf{L}^{(i)}$, where $r_i = 2^i$ for $i = 0, \dots, L-1$. The final high-frequency prior is obtained by accumulating residuals across scales:

$$\mathbf{P}_{\text{hf}} = \sum_{i=0}^{L-1} \mathbf{H}^{(i)}. \quad (4)$$

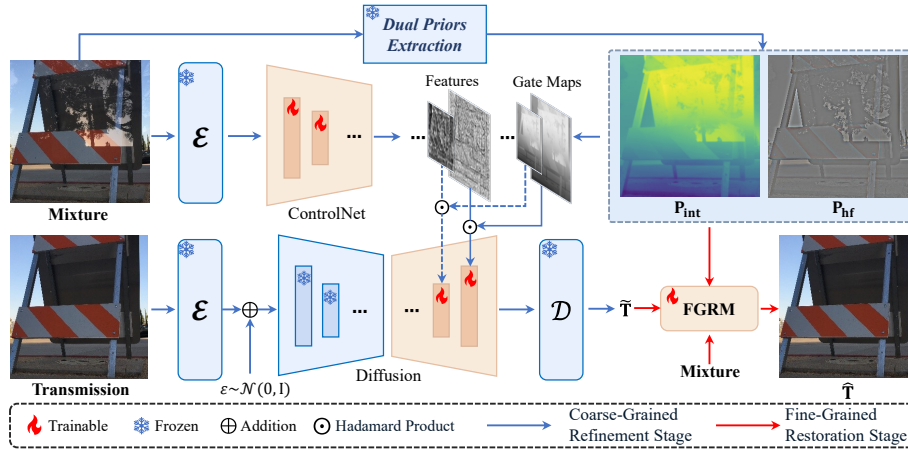


Fig. 3: The framework of the proposed **FUMO** method. Given a mixed image \mathbf{M} , we obtain two priors \mathbf{P}_{int} and \mathbf{P}_{hf} through dual priors extraction. A diffusion-based backbone performs conditional denoising, where the extracted features and gates are injected through element-wise fusion operations to guide multi-scale feature aggregation. The decoder produces a coarse restoration, which is further refined by the trainable fine-grained refinement module (FGRM).

By aggregating residual components from fine to coarse scales, \mathbf{P}_{hf} captures detail responses that are informative for structure awareness, while remaining simple and efficient to compute. We further clamp and linearly rescale the extracted response to $[0, 1]$ at the input resolution for stable conditioning. Combined with the intensity prior, it forms a complementary pair of explicit signals that will be integrated into the subsequent gated modulation design.

3.2 Prior-modulated diffusion framework for SIRR

We propose a prior-modulated diffusion framework for single image reflection removal (FUMO), as illustrated in Fig. 3. Our architecture follows a coarse-to-fine design, consisting of a coarse restoration diffusion and a fine-grained refinement module. The coarse stage adopts a ControlNet-conditioned [55] diffusion denoiser, where perceptual priors are incorporated through a gated modulation mechanism for spatially adaptive conditioning. The refinement module further enhances geometric consistency and restores fine structural details, producing the final high-quality transmission image.

Coarse-Grained Restoration Diffusion Model. The coarse stage targets strong reflection suppression to obtain an initial transmission estimate that is faithful in global appearance and low-frequency structure. We adopt a pretrained T2I diffusion model as the backbone, such as stable diffusion [33], which provides

strong generative priors. The VAE encoder takes the mixed image \mathbf{M} and transmission image \mathbf{T} as input to generate latent tensors $z_{\mathbf{M}}$ and $z_{\mathbf{T}}$, respectively. ControlNet takes $z_{\mathbf{M}}$ as input to guide the SD model output. The diffusion denoiser μ_{θ} receives noisy input $z_t = \alpha_t z_{\mathbf{T}} + \sigma_t \epsilon$ (t denotes diffusion step, α_t and σ_t are determined by noise scheduler with $\epsilon \sim \mathcal{N}(0, \mathbf{I})$), and the control signal $c_m = f_{\phi}(\mathbf{M})$ from ControlNet f_{ϕ} to predict the latent $z_0 = z_{\mathbf{T}}$. Following [48, 53], we adopt a one-step denoising formulation for the coarse restoration stage.

Gated Modulation Module. The intensity prior \mathbf{P}_{int} and the high-frequency prior \mathbf{P}_{hf} provide complementary guidance for spatially controllable restoration. \mathbf{P}_{int} indicates where reflections are severe and thus require stronger conditional intervention, while \mathbf{P}_{hf} highlights regions with active fine structures where the conditioning should be applied with higher sensitivity to preserve details. We combine them to construct a spatial gate that selectively strengthens the conditioning in locations that are simultaneously dominated by reflection and structurally rich.

Specifically, we define the gate map as

$$\mathbf{g} = \mathbf{1} + \beta \mathbf{P}_{\text{int}} \odot \mathbf{P}_{\text{hf}}, \quad (5)$$

where \odot denotes element-wise multiplication and β controls the overall modulation strength. The additive identity term ensures that the mechanism reduces to standard conditioning when either guidance signal is weak, while the multiplicative interaction emphasizes their joint presence.

The gate is applied in the coarse stage to modulate the residual injection from the conditioning branch into the restoration network. Let $\mathbf{c}_m = \{\mathbf{c}_s\}$ denote the multi-scale residual tensors produced by ControlNet, where s indexes the injection scale. For each scale, we resize \mathbf{g} to match the spatial resolution of \mathbf{c}_s and perform elementwise modulation to generate the gated modulation condition signal $\tilde{\mathbf{c}}_s$:

$$\tilde{\mathbf{c}}_s = \text{clip}(\mathcal{I}_s(\mathbf{g}), 1, 1 + \beta_{\text{max}}) \odot \mathbf{c}_s, \quad (6)$$

where $\mathcal{I}_s(\cdot)$ denotes per-scale interpolation for alignment and $\text{clip}(\cdot)$ clamps the gate to a bounded range for stable injection. In practice, β is warmed up and then increased to β_{max} during training, so that the gated modulation is introduced progressively. We set $\beta_{\text{max}} = 0.25$ and use a warmup ratio of 0.1 empirically.

Fine-Grained Refinement Module. Although the coarse stage provides strong reflection suppression, its aggressive restoration may introduce geometric drift or local structural inconsistency, especially in regions where transmission structures are tightly entangled with reflections. To improve geometric coherence and recover fine details, we develop a fine-grained refinement module (FGRM) as a deterministic refiner operating in the image space.

The refinement module takes the coarse prediction together with the original mixture and the guidance signals as inputs. Let $\hat{\mathbf{T}}$ denote the decoded transmission image obtained in the coarse stage. The refiner receives the channel-wise concatenation

$$\hat{\mathbf{T}} = R_\phi(\text{concat}(\mathbf{M}, \tilde{\mathbf{T}}, \mathbf{P}_{\text{hf}}, \mathbf{P}_{\text{int}})), \quad (7)$$

where R_ϕ denotes the Fine-Grained Refinement Module. In practice, we adopt a U-Net but replace the standard activation with a lightweight channel gating operation that splits features into two halves and multiplies them element-wise, which is called SimpleGate in NAFNet [6].

3.3 Training Strategy

The coarse-to-fine design is optimized separately with stage-specific objectives. The coarse stage focuses on one-step latent restoration under guided and gated modulation, while the refinement stage operates deterministically in the image space to improve geometric consistency and recover fine structures.

Coarse-Grained Restoration Stage. In the backward denoising process, the traditional diffusion models predict the noise at randomly sampled step t , the corresponding multi-step training loss is formulated as:

$$\mathcal{L}_{\text{ldm}} = \|\epsilon - \mu_\theta(z_t, t, \tilde{\mathbf{c}}_m)\|_2^2. \quad (8)$$

where $\tilde{\mathbf{c}}_m$ is the control signal from ControlNet and gated modulation.

Following [12, 48, 53], we adopt one-step denoising for stable and efficient restoration. Instead of predicting noise, the network directly regresses a less perturbed latent. Specifically, for a target timestep t (with a smaller t indicating a cleaner latent), the model takes a maximally perturbed latent z_N as input and predicts z_t in a single forward pass:

$$\mathcal{L}_{\text{coarse}} = \|z_t - \mu_\theta(z_N, t, \tilde{\mathbf{c}}_m)\|_2^2. \quad (9)$$

During training, t is sampled uniformly and N is set to 1000. At inference time, $t = 0$ is set to obtain $\hat{z}_{\mathbf{T}} = \mu_\theta(z_N, 0, \tilde{\mathbf{c}}_m)$ with $z_N \sim \mathcal{N}(0, I)$, and $\hat{z}_{\mathbf{T}}$ is decoded to produce the restored transmission image.

In this training stage, only the ControlNet and the upsampling blocks of denoising U-Net are optimized. The VAE and the remaining parameters of U-Net are kept frozen to preserve the pretrained generative prior and stabilize optimization.

Fine-Grained Refinement Stage. The Fine-Grained Refinement Module refines the coarse prediction in the image space. Denoting the refined output by $\hat{\mathbf{T}}$ and the ground-truth transmission by \mathbf{T} , we employ a composite objective that balances pixel fidelity, perceptual similarity and geometric consistency. In this training stage, only the Fine-Grained Refinement Module is updated.

A pixel-level reconstruction loss constrains the global color and luminance:

$$\mathcal{L}_{\text{pix}} = \|\hat{\mathbf{T}} - \mathbf{T}\|_1. \quad (10)$$

Then we include a perceptual loss based on LPIPS [56] to discourage over-smoothing and to better preserve visually salient structures:

$$\mathcal{L}_{\text{perc}} = \mathcal{L}_{\text{LPIPS}}(\hat{\mathbf{T}}, \mathbf{T}) = \sum_i w_i \|\phi_i(\hat{\mathbf{T}}) - \phi_i(\mathbf{T})\|_2, \quad (11)$$

where $\phi_i(\cdot)$ denotes the feature map extracted from the i -th layer of AlexNet [18]. Finally, to explicitly promote edge alignment and mitigate local misalignment artifacts, we impose an edge-aware gradient loss and measure the discrepancy of both horizontal and vertical derivatives:

$$\mathcal{L}_{\text{grad}} = \|\nabla_x \hat{\mathbf{T}} - \nabla_x \mathbf{T}\|_1 + \|\nabla_y \hat{\mathbf{T}} - \nabla_y \mathbf{T}\|_1 \quad (12)$$

where $\nabla(\cdot)$ denotes image gradients computed by fixed Sobel filters.

Gathering all the loss terms yields the refinement objective as:

$$\mathcal{L}_{\text{refine}} = \lambda_{\text{pix}} \mathcal{L}_{\text{pix}} + \lambda_{\text{perc}} \mathcal{L}_{\text{perc}} + \lambda_{\text{grad}} \mathcal{L}_{\text{grad}}, \quad (13)$$

where the weights $\lambda_{\text{pix}} = 0.5$, $\lambda_{\text{perc}} = 0.25$, and $\lambda_{\text{grad}} = 0.25$ are set empirically.

4 Experiments

4.1 Implementation Details

We implement the proposed method in PyTorch [30]. All experiments are conducted on 4 NVIDIA GeForce RTX 4090 GPUs with a batch size of 1. The two stages are trained separately, with 100k steps and 10k steps respectively. In coarse stage, we initialize the U-Net and ControlNet with pretrained weights of Stable Diffusion V2.1 [33], and update the weights using AdamW [17] with a learning rate of 5×10^{-5} . In refinement stage, we freeze the coarse restoration part and train the fine-grain refinement module using AdamW with a learning rate of 1×10^{-4} .

Datasets Training uses a combination of real paired data and synthetic data. The real subset contains 89 image pairs from Real [57], 200 pairs from Nature [22], 1230 pairs from RR4k [4], 6600 pairs from RRW [62] and 23303 pairs from DRR [12]. The remaining image pairs from Real and Nature are used for evaluation. For synthetic data, we generate 16120 training pairs by blending images sampled independently from the COCO [25] dataset, using formulation from DSRNet [14] $M = \gamma_1 T + \gamma_2 R - \gamma_1 \gamma_2 T \odot R$. Following [58], we sample γ_1 and γ_2 for 3 channels individually. During training, all images are resized and randomly cropped to a resolution of 768, with random flipping and color jitter applied for augmentation.

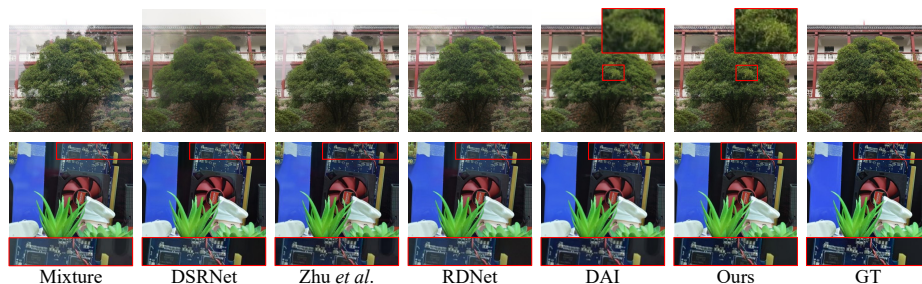


Fig. 4: Qualitative comparisons on representative examples from the three benchmarks. The red rectangles highlight key regions for comparison.

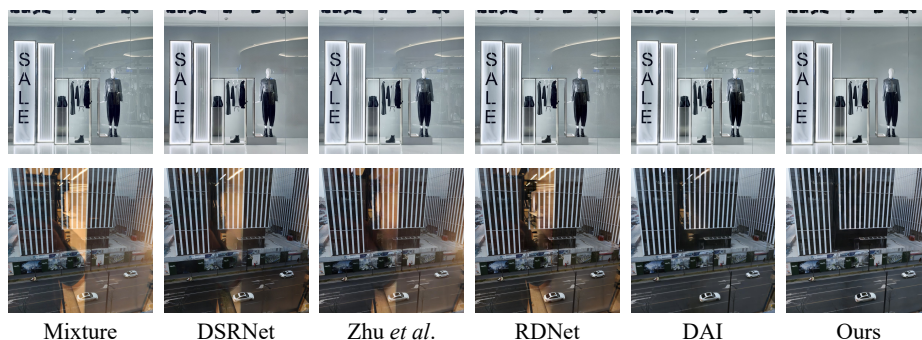


Fig. 5: Qualitative comparisons on challenging real-world mixed images.

4.2 Comparison with State-of-the-arts

We evaluate reflection removal on three widely used real benchmarks, including Nature [22], Real [57], and SIR2 [37], following their standard test splits and evaluation protocols. To assess robustness under unconstrained imaging conditions, we further report qualitative results on a small set of in the wild mixed images collected from the Internet, which exhibit diverse reflection patterns and challenging scene content. We compare our method with representative single image reflection removal approaches, including IBCLN [22], Dong *et al.* [7], YTMT [13], DSRNet [14], Zhu *et al.* [62], RDNet [58] and DAI [12]. For methods with publicly available training code, we follow the official implementations and finetune them on our training data to reduce the impact of mismatched data distributions. All competing methods are evaluated using the same test images and the same preprocessing pipeline.

Quantitative Comparison. In quantitative evaluation, we employ PSNR [15] and SSIM [43] to measure fidelity with respect to the ground truth transmission, together with LPIPS [56] for perceptual similarity. We additionally report CLIP-

Table 1: Quantitative comparisons on three reflection removal benchmarks (Nature, Real, and SIR²). For each evaluation metric, the arrow \uparrow (\downarrow) indicates that larger (smaller) values are better. The best results are highlighted in **bold**, and the second-best results are underlined.

Dataset (size)	Metric	Method							
		IBCLN	Dong <i>et al.</i>	YTMT	DSRNet	Zhu <i>et al.</i>	RDNet	DAI	Ours
Nature (20)	PSNR \uparrow	23.77	23.33	20.76	24.58	25.68	25.74	<u>26.81</u>	26.93
	SSIM \uparrow	0.786	0.812	0.768	0.817	0.826	<u>0.828</u>	0.840	0.840
	LPIPS \downarrow	0.145	0.117	0.183	0.120	<u>0.103</u>	0.109	0.203	0.088
	CLIPQA \uparrow	0.408	0.419	0.400	0.440	0.432	0.431	0.362	<u>0.439</u>
	MUSIQ \uparrow	58.83	59.56	59.63	<u>62.09</u>	61.37	60.26	54.70	62.87
Real (20)	PSNR \uparrow	21.55	22.34	22.87	23.37	21.85	24.81	<u>25.21</u>	25.95
	SSIM \uparrow	0.767	0.811	0.808	0.801	0.781	<u>0.838</u>	<u>0.838</u>	0.852
	LPIPS \downarrow	0.210	0.150	0.157	0.157	0.183	<u>0.118</u>	0.150	0.097
	CLIPQA \uparrow	0.444	0.441	0.464	0.483	0.453	0.538	0.414	<u>0.509</u>
	MUSIQ \uparrow	58.08	57.55	58.72	60.44	58.46	<u>61.42</u>	58.20	62.12
SIR ² (500)	PSNR \uparrow	23.89	24.29	23.73	25.51	25.37	26.46	27.35	<u>27.22</u>
	SSIM \uparrow	0.886	0.902	0.891	0.913	0.904	0.921	<u>0.923</u>	0.925
	LPIPS \downarrow	0.127	0.099	0.119	0.094	0.112	<u>0.080</u>	0.093	0.067
	CLIPQA \uparrow	0.384	0.394	0.385	0.405	<u>0.408</u>	0.396	0.365	0.419
	MUSIQ \uparrow	58.16	57.55	58.09	<u>58.82</u>	58.11	58.53	54.40	59.85
Average (540)	PSNR \uparrow	23.79	24.17	23.57	25.39	25.24	26.36	27.24	<u>27.15</u>
	SSIM \uparrow	0.877	0.895	0.882	0.905	0.896	0.914	<u>0.916</u>	0.918
	LPIPS \downarrow	0.131	0.102	0.123	0.098	0.114	<u>0.083</u>	0.100	0.069
	CLIPQA \uparrow	0.387	0.397	0.388	0.410	<u>0.411</u>	0.403	0.367	0.424
	MUSIQ \uparrow	58.19	57.63	58.18	<u>59.02</u>	58.26	58.71	54.57	59.88

IQA [39] and MUSIQ [16] as a no reference perceptual quality indicator to complement full reference metrics. Quantitative results are summarized in Tab. 1. Across the three benchmarks, our method achieves consistently strong performance on both distortion oriented metrics (PSNR/SSIM) and perceptual metrics (LPIPS/CLIPQA/MUSIQ), indicating effective reflection suppression without sacrificing structural fidelity. In particular, the gains are most pronounced in perceptual metrics such as LPIPS and MUSIQ, indicating that the proposed guidance and gated modulation improve visual quality while better preserving transmission structures under complex reflections.

Qualitative Comparison. Fig. 4 shows qualitative comparisons on representative examples from the three benchmarks. In addition, Fig. 5 presents results on extra real-world mixed images, including photos captured by us and images collected from the Internet, to further assess robustness under diverse reflection conditions. The results demonstrate that previous methods often struggle under complex reflections, leading to residual reflection traces, local over smoothing, or color inconsistencies. In contrast, our results better retain geometric coher-



Fig. 6: Qualitative ablation results on gated modulation.

ence and fine structures, particularly around edges and textured regions, while removing reflection patterns that are entangled with transmission content.

4.3 Ablation Study

Ablation on Gated Modulation. This part isolates the role of gated modulation in the coarse stage, where conditional residual injections are spatially modulated before entering the diffusion denoiser. All variants share the same training methods, and the only change lies in how the gate is formed from the guidance signals. Specifically, we compare: (i) *w/o gate*, where the injection tensors are passed without modulation ($g \equiv 1$); (ii) *intensity only*, where the gate is driven solely by the intensity prior ($g = 1 + \beta P_{\text{int}}$); (iii) *high-frequency only*, where the gate is driven solely by the high-frequency prior ($g = 1 + \beta P_{\text{hf}}$); and (iv) *full*, where the gate combines both signals as in Eq. (5). Tab. 2 reports quantitative results on the same benchmarks and metrics as in Sec. 4.2, and Fig. 6 provides representative visual comparisons.

Across datasets, removing gated modulation degrades perceptual quality most noticeably and the outputs exhibit more residual reflection artifacts and more obvious restoration traces in Fig. 6. Using a single guidance signal partially alleviates these artifacts, but the two priors emphasize different failure modes. The intensity driven gate primarily improves suppression in high severity regions, whereas the high-frequency driven gate better preserves fine structures and edge sharpness. Combining P_{int} and P_{hf} in the gate consistently gives the most favorable perceptual scores among the variants and produces cleaner reflection removal with more faithful transmission structures, supporting the design choice of modulating coarse stage injections with a severity aware and detail sensitive signal.

Ablation on Refinement module. This experiment examines the contribution of the Fine-Grained Refinement by comparing the full pipeline with two

Table 2: Quantitative ablation results on gated modulation and refinement module. For each evaluation metric, the arrow \uparrow (\downarrow) indicates that larger (smaller) values are better. The best results are highlighted in **bold**. HF-only refers to *high-frequency only* variant

Metric	Abl. on gated modulation			Abl. on refinement module		Ours
	W/o gate	Intensity-only	HF-only	Coarse-only	Fine-decoder	
PSNR \uparrow	26.55	26.94	26.78	26.27	26.75	27.15
SSIM \uparrow	0.897	0.905	0.906	0.865	0.891	0.918
LPIPS \downarrow	0.076	0.073	0.071	0.133	0.084	0.069
CLIPQA \uparrow	0.390	0.403	0.393	0.385	0.398	0.424
MUSIQ \uparrow	57.13	58.40	58.08	57.56	58.43	59.88

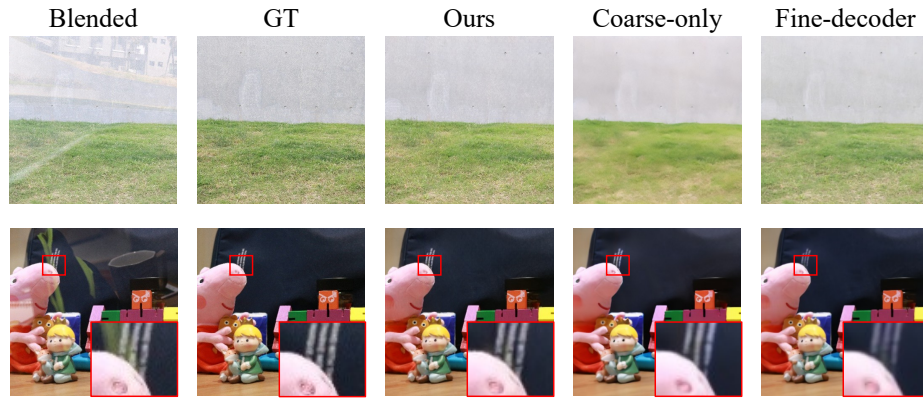


Fig. 7: Qualitative ablation results on refinement module.

variants: (i) *coarse-only* variant and (ii) *fine-decoder* variant. While the *coarse-only* variant directly decodes the Coarse-Grained Restoration output as the final prediction, the *fine-decoder* variant utilizes a fine-tuned decoder following the training protocol in DAI [12]. All settings use the same coarse model.

As summarized in Tab. 2 and illustrated in Fig. 7, the *coarse-only* variant is already effective at suppressing dominant reflections, confirming the capability of the one-step coarse restoration. However, its outputs often exhibit noticeably reduced sharpness and visible restoration traces, particularly around edges and textured regions where reflection patterns intertwine with transmission structures. With a fine-tuned decoder, *fine-decoder* variant shows partial improvements in artifact removal and detail enhancement, but falls short of fully addressing the underlying problem. Introducing the refinement module largely improves visual clarity and structural coherence. Residual blur and local artifacts are substantially reduced. These observations support the role of the refinement network as a deterministic correction step that consolidates the coarse restoration into a sharper and more geometrically consistent transmission estimate.

5 Conclusion

This paper proposed a diffusion framework for single image reflection removal that improves controllability and structural faithfulness under spatially varying reflections. The method derives two guidance priors from the mixed image and uses them to guide restoration in a complementary manner. The coarse stage applies gated modulation to strengthen reflection suppression where it is needed and to better preserve transmission structures in detail sensitive regions. The refinement module improves geometric consistency and visual clarity and reduces blur and restoration traces. Experiments on standard benchmarks and additional real world mixtures show competitive performance and clear improvements on perceptual quality measures.

References

1. Agrawal, A., Raskar, R., Nayar, S.K., Li, Y.: Removing photography artifacts using gradient projection and flash-exposure sampling. In: ACM SIGGRAPH 2005 Papers, pp. 828–835 (2005)
2. Arvanitopoulos, N., Achanta, R., Susstrunk, S.: Single image reflection suppression. In: Proceedings of the IEEE Conference on Computer Vision and Pattern Recognition (CVPR) (July 2017)
3. Bai, S., Chen, K., Liu, X., Wang, J., Ge, W., Song, S., Dang, K., Wang, P., Wang, S., Tang, J., Zhong, H., Zhu, Y., Yang, M., Li, Z., Wan, J., Wang, P., Ding, W., Fu, Z., Xu, Y., Ye, J., Zhang, X., Xie, T., Cheng, Z., Zhang, H., Yang, Z., Xu, H., Lin, J.: Qwen2.5-vl technical report. arXiv preprint arXiv:2502.13923 (2025)
4. Chen, G.Y., Zheng, C.W., Fan, G., Su, J.N., Gan, M., Chen, C.P.: Real-world image reflection removal: An ultra-high-definition dataset and an efficient baseline. *IEEE Transactions on Circuits and Systems for Video Technology* **35**(5), 4397–4408 (2024)
5. Chen, L., Bai, S., Chai, W., Xie, W., Zhao, H., Vinci, L., Lin, J., Chang, B.: Multimodal representation alignment for image generation: Text-image interleaved control is easier than you think. arXiv preprint arXiv:2502.20172 (2025)
6. Chen, L., Chu, X., Zhang, X., Sun, J.: Simple baselines for image restoration. In: European conference on computer vision. pp. 17–33. Springer (2022)
7. Dong, Z., Xu, K., Yang, Y., Bao, H., Xu, W., Lau, R.W.: Location-aware single image reflection removal. In: Proceedings of the IEEE/CVF international conference on computer vision. pp. 5017–5026 (2021)
8. Han, B.J., Sim, J.Y.: Reflection removal using low-rank matrix completion. In: Proceedings of the IEEE Conference on Computer Vision and Pattern Recognition. pp. 5438–5446 (2017)
9. He, K., Sun, J., Tang, X.: Guided image filtering. *IEEE transactions on pattern analysis and machine intelligence* **35**(6), 1397–1409 (2012)
10. Ho, J., Jain, A., Abbeel, P.: Denoising diffusion probabilistic models. *Advances in neural information processing systems* **33**, 6840–6851 (2020)
11. Hong, Y., Zhong, H., Weng, S., Liang, J., Shi, B.: L-differ: Single image reflection removal with language-based diffusion model. In: European Conference on Computer Vision. pp. 58–76. Springer (2024)

12. Hu, J., Yang, C., Zhou, Z., Fang, J., Yang, X., Tian, Q., Shen, W.: Dereflexion any image with diffusion priors and diversified data. arXiv preprint arXiv:2503.17347 (2025)
13. Hu, Q., Guo, X.: Trash or treasure? an interactive dual-stream strategy for single image reflection separation. *Advances in Neural Information Processing Systems* **34**, 24683–24694 (2021)
14. Hu, Q., Guo, X.: Single image reflection separation via component synergy. In: *Proceedings of the IEEE/CVF international conference on computer vision*. pp. 13138–13147 (2023)
15. Huynh-Thu, Q., Ghanbari, M.: Scope of validity of psnr in image/video quality assessment. *Electronics letters* **44**(13), 800–801 (2008)
16. Ke, J., Wang, Q., Wang, Y., Milanfar, P., Yang, F.: Musiq: Multi-scale image quality transformer. In: *Proceedings of the IEEE/CVF international conference on computer vision*. pp. 5148–5157 (2021)
17. Kingma, D.P.: Adam: A method for stochastic optimization. arXiv preprint arXiv:1412.6980 (2014)
18. Krizhevsky, A., Sutskever, I., Hinton, G.E.: Imagenet classification with deep convolutional neural networks. *Advances in neural information processing systems* **25** (2012)
19. Lei, C., Chen, Q.: Robust reflection removal with reflection-free flash-only cues. In: *Proceedings of the IEEE/CVF Conference on Computer Vision and Pattern Recognition*. pp. 14811–14820 (2021)
20. Lei, C., Huang, X., Zhang, M., Yan, Q., Sun, W., Chen, Q.: Polarized reflection removal with perfect alignment in the wild. In: *Proceedings of the IEEE/CVF conference on computer vision and pattern recognition*. pp. 1750–1758 (2020)
21. Levin, A., Weiss, Y.: User assisted separation of reflections from a single image using a sparsity prior. *IEEE Transactions on Pattern Analysis and Machine Intelligence* **29**(9), 1647–1654 (2007)
22. Li, C., Yang, Y., He, K., Lin, S., Hopcroft, J.E.: Single image reflection removal through cascaded refinement. In: *Proceedings of the IEEE/CVF conference on computer vision and pattern recognition*. pp. 3565–3574 (2020)
23. Li, Y., Liu, M., Yi, Y., Li, Q., Ren, D., Zuo, W.: Two-stage single image reflection removal with reflection-aware guidance. *Applied Intelligence* **53**(16), 19433–19448 (2023)
24. Li, Z., Wu, X., Du, H., Liu, F., Nghiem, H., Shi, G.: A survey of state of the art large vision language models: Alignment, benchmark, evaluations and challenges. arXiv preprint arXiv:2501.02189 (2025)
25. Lin, T.Y., Maire, M., Belongie, S., Hays, J., Perona, P., Ramanan, D., Dollár, P., Zitnick, C.L.: Microsoft coco: Common objects in context. In: *European conference on computer vision*. pp. 740–755. Springer (2014)
26. Lin, X., Yu, F., Hu, J., You, Z., Shi, W., Ren, J.S., Gu, J., Dong, C.: Harnessing diffusion-yielded score priors for image restoration. arXiv preprint arXiv:2507.20590 (2025)
27. Liu, S., Han, Y., Xing, P., Yin, F., Wang, R., Cheng, W., Liao, J., Wang, Y., Fu, H., Han, C., et al.: Step1x-edit: A practical framework for general image editing. arXiv preprint arXiv:2504.17761 (2025)
28. Liu, Y., Ma, X., Bailey, J., Lu, F.: Reflection backdoor: A natural backdoor attack on deep neural networks. In: *European Conference on Computer Vision*. pp. 182–199. Springer (2020)
29. Nichol, A.Q., Dhariwal, P.: Improved denoising diffusion probabilistic models. In: *International conference on machine learning*. pp. 8162–8171. PMLR (2021)

30. Paszke, A., Gross, S., Massa, F., Lerer, A., Bradbury, J., Chanan, G., Killeen, T., Lin, Z., Gimelshein, N., Antiga, L., et al.: Pytorch: An imperative style, high-performance deep learning library. *Advances in neural information processing systems* **32** (2019)
31. Peebles, W., Xie, S.: Scalable diffusion models with transformers. In: *Proceedings of the IEEE/CVF international conference on computer vision*. pp. 4195–4205 (2023)
32. Podell, D., English, Z., Lacey, K., Blattmann, A., Dockhorn, T., Müller, J., Penna, J., Rombach, R.: Sdxl: Improving latent diffusion models for high-resolution image synthesis. *arXiv preprint arXiv:2307.01952* (2023)
33. Rombach, R., Blattmann, A., Lorenz, D., Esser, P., Ommer, B.: High-resolution image synthesis with latent diffusion models. In: *Proceedings of the IEEE/CVF conference on computer vision and pattern recognition*. pp. 10684–10695 (2022)
34. Shih, Y., Krishnan, D., Durand, F., Freeman, W.T.: Reflection removal using ghosting cues. In: *Proceedings of the IEEE conference on computer vision and pattern recognition*. pp. 3193–3201 (2015)
35. Simon, C., Kyu Park, I.: Reflection removal for in-vehicle black box videos. In: *Proceedings of the IEEE Conference on Computer Vision and Pattern Recognition (CVPR) (June 2015)*
36. Szeliski, R., Avidan, S., Anandan, P.: Layer extraction from multiple images containing reflections and transparency. In: *Proceedings IEEE Conference on Computer Vision and Pattern Recognition. CVPR 2000 (Cat. No. PR00662)*. vol. 1, pp. 246–253. IEEE (2000)
37. Wan, R., Shi, B., Duan, L.Y., Tan, A.H., Kot, A.C.: Benchmarking single-image reflection removal algorithms. In: *Proceedings of the IEEE international conference on computer vision*. pp. 3922–3930 (2017)
38. Wan, R., Shi, B., Li, H., Duan, L.Y., Kot, A.C.: Face image reflection removal. *International Journal of Computer Vision* **129**(2), 385–399 (2021)
39. Wang, J., Chan, K.C., Loy, C.C.: Exploring clip for assessing the look and feel of images. In: *Proceedings of the AAAI conference on artificial intelligence*. vol. 37, pp. 2555–2563 (2023)
40. Wang, J., Yue, Z., Zhou, S., Chan, K.C., Loy, C.C.: Exploiting diffusion prior for real-world image super-resolution. *International Journal of Computer Vision* **132**(12), 5929–5949 (2024)
41. Wang, R., Zheng, Y., Zhang, Z., Li, C., Liu, S., Zhai, G., Liu, X.: Learning hazing to dehazing: Towards realistic haze generation for real-world image dehazing. In: *Proceedings of the Computer Vision and Pattern Recognition Conference*. pp. 23091–23100 (2025)
42. Wang, W., Gao, Z., Gu, L., Pu, H., Cui, L., Wei, X., Liu, Z., Jing, L., Ye, S., Shao, J., et al.: Internvl3. 5: Advancing open-source multimodal models in versatility, reasoning, and efficiency. *arXiv preprint arXiv:2508.18265* (2025)
43. Wang, Z., Simoncelli, E.P., Bovik, A.C.: Multiscale structural similarity for image quality assessment. In: *The thirty-seventh Asilomar conference on signals, systems & computers, 2003*. vol. 2, pp. 1398–1402. IEEE (2003)
44. Wei, H., Xu, B., Liu, H., Wu, S., Liu, J., Peng, Y., Wang, P., Liu, Z., He, J., Xietian, Y., et al.: Skywork unipic 2.0: Building kontekst model with online rl for unified multimodal model. *arXiv preprint arXiv:2509.04548* (2025)
45. Wei, K., Yang, J., Fu, Y., Wipf, D., Huang, H.: Single image reflection removal exploiting misaligned training data and network enhancements. In: *Proceedings of the IEEE/CVF Conference on Computer Vision and Pattern Recognition*. pp. 8178–8187 (2019)

46. Wu, H., Zhang, Z., Zhang, W., Chen, C., Liao, L., Li, C., Gao, Y., Wang, A., Zhang, E., Sun, W., et al.: Q-align: Teaching llms for visual scoring via discrete text-defined levels. arXiv preprint arXiv:2312.17090 (2023)
47. Wu, R., Sun, L., Ma, Z., Zhang, L.: One-step effective diffusion network for real-world image super-resolution. *Advances in Neural Information Processing Systems* **37**, 92529–92553 (2024)
48. Xu, G., Ge, Y., Liu, M., Fan, C., Xie, K., Zhao, Z., Chen, H., Shen, C.: What matters when repurposing diffusion models for general dense perception tasks? arXiv preprint arXiv:2403.06090 (2024)
49. Xue, T., Rubinstein, M., Liu, C., Freeman, W.T.: A computational approach for obstruction-free photography. *ACM Transactions on Graphics (TOG)* **34**(4), 1–11 (2015)
50. Yang, J., Li, H., Dai, Y., Tan, R.T.: Robust optical flow estimation of double-layer images under transparency or reflection. In: *Proceedings of the IEEE Conference on Computer Vision and Pattern Recognition*. pp. 1410–1419 (2016)
51. Yang, K., Cai, J., Ouyang, L., Vasluianu, F.A., Timofte, R., Ding, J., Sun, H., Fu, L., Li, J., Ho, C.M., Meng, Z., Li, M., Wang, H., Hu, Q., Wang, J., Zhao, H., Hu, J., Guo, X., Yang, M., He, J., Wang, Y., Chen, Z., Fang, H., Zhang, W., Cong, R., Hegde, D.D., Kalal, J., Akalwadi, N., Tabib, R.A., Mudenagudi, U., Lin, Y.F., Lee, C.M., Hsu, C.C., Zhang, M., Nathan, S., Uma, K., Sasithradevi, A., Bama, B.S., Roomi, S.M.M., Benjdira, B., Ali, A.M., Boulila, W., Dong, W., Li, Y., Hussein, A., Zhou, H., Chen, J., Xiao, Z., Li, Z.: Ntire 2025 challenge on single image reflection removal in the wild: Datasets, methods and results. In: *Proceedings of the IEEE/CVF Conference on Computer Vision and Pattern Recognition (CVPR) Workshops*. pp. 1301–1311 (June 2025)
52. Yao, M., Wang, M., Tam, K.M., Li, L., Xue, T., Gu, J.: Polarfree: Polarization-based reflection-free imaging. In: *Proceedings of the Computer Vision and Pattern Recognition Conference*. pp. 10890–10899 (2025)
53. Ye, C., Qiu, L., Gu, X., Zuo, Q., Wu, Y., Dong, Z., Bo, L., Xiu, Y., Han, X.: Stablenormal: Reducing diffusion variance for stable and sharp normal. *ACM Transactions on Graphics (TOG)* **43**(6), 1–18 (2024)
54. Yu, F., Koltun, V.: Multi-scale context aggregation by dilated convolutions. arXiv preprint arXiv:1511.07122 (2015)
55. Zhang, L., Rao, A., Agrawala, M.: Adding conditional control to text-to-image diffusion models. In: *Proceedings of the IEEE/CVF international conference on computer vision*. pp. 3836–3847 (2023)
56. Zhang, R., Isola, P., Efros, A.A., Shechtman, E., Wang, O.: The unreasonable effectiveness of deep features as a perceptual metric. In: *Proceedings of the IEEE conference on computer vision and pattern recognition*. pp. 586–595 (2018)
57. Zhang, X., Ng, R., Chen, Q.: Single image reflection separation with perceptual losses. In: *Proceedings of the IEEE conference on computer vision and pattern recognition*. pp. 4786–4794 (2018)
58. Zhao, H., Li, M., Hu, Q., Guo, X.: Reversible decoupling network for single image reflection removal. In: *Proceedings of the Computer Vision and Pattern Recognition Conference*. pp. 26430–26439 (2025)
59. Zheng, Q., Shi, B., Chen, J., Jiang, X., Duan, L.Y., Kot, A.C.: Single image reflection removal with absorption effect. In: *Proceedings of the IEEE/CVF conference on computer vision and pattern recognition*. pp. 13395–13404 (2021)
60. Zhong, H., Hong, Y., Weng, S., Liang, J., Shi, B.: Language-guided image reflection separation. In: *Proceedings of the IEEE/CVF Conference on Computer Vision and Pattern Recognition*. pp. 24913–24922 (2024)

61. Zhou, H., Dong, W., Liu, X., Zhang, Y., Zhai, G., Chen, J.: Low-light image enhancement via generative perceptual priors. In: Proceedings of the AAAI Conference on Artificial Intelligence. vol. 39, pp. 10752–10760 (2025)
62. Zhu, Y., Fu, X., Jiang, P.T., Zhang, H., Sun, Q., Chen, J., Zha, Z.J., Li, B.: Revisiting single image reflection removal in the wild. In: Proceedings of the IEEE/CVF Conference on Computer Vision and Pattern Recognition. pp. 25468–25478 (2024)